



Facet-controlled Pt-Ir nanocrystals with substantially enhanced activity and durability towards oxygen reduction

Jiawei Zhu ^{1,2,†}, Ahmed O. Elnabawy ^{3,†}, Zhiheng Lyu ⁴, Minghao Xie ⁴, Ellen A. Murray ³, Zitao Chen ¹, Wanqin Jin ², Manos Mavrikakis ^{3,*,‡}, Younan Xia ^{1,4,*,¶}

Nanocrystals made of Pt–Ir alloys are fascinating catalysts towards the oxygen reduction reaction (ORR), but the lack of control over their surface atomic structures hinders further optimization of their catalytic performance. Here we report, for the first time, a class of highly active and durable ORR catalysts based on Pd@Pt–Ir nanocrystals with well-controlled facets. With an average of 1.6 atomic layers of a Pt₄Ir alloy on the surface, the nanocrystals can be made in cubic, octahedral, and icosahedral shapes to present Pt–Ir $\{1\ 0\ 0\}$, $\{1\ 1\ 1\}$, and $\{1\ 1\ 1\}$ plus twin boundaries, respectively. The Pd@Pt–Ir nanocrystals exhibit not only facet-dependent catalytic properties but also substantially enhanced ORR activity and durability relative to a commercial Pt/C and their Pd@Pt counterparts. Among them, the Pd@Pt–Ir icosahedra deliver the best performance, with a mass activity of 1.88 A·mg $_{\rm Pt}^{-1}$ at 0.9 V, which is almost 15 times that of the commercial Pt/C. Our density functional theory (DFT) calculations attribute the high activity of the Pd@Pt–Ir nanocrystals, and the facet dependence of these activities, to easier protonation of O* and OH* under relevant OH* coverages, relative to the corresponding energetics on clean Pd@Pt surfaces. The DFT calculations also indicate that incorporating Ir atoms into the Pt lattice destabilizes OH–OH interactions on the surface, thereby raising the oxidation potential of Pt and greatly improving the catalytic durability.

Introduction

Primarily owing to the acidic and oxidizing environment, together with the slow kinetics of oxygen reduction reaction (ORR) in a polymer electrolyte membrane fuel cell (PEMFC), a Pt-based catalyst has to be deposited on the cathode in order to accelerate the ORR and thereby maintain the performance of

¹ The Wallace H. Coulter Department of Biomedical Engineering, Georgia Institute of Technology and Emory University, Atlanta, GA 30332, United States ² State Key Laboratory of Materials-Oriented Chemical Engineering, College of Chemical Engineering, Nanjing Tech University, Nanjing, Jiangsu 211816, PR China

³ Department of Chemical and Biological Engineering, University of Wisconsin-Madison, Madison, WI 53706, United States

⁴ School of Chemistry and Biochemistry, Georgia Institute of Technology, Atlanta, GA 30332, United States

such a device [1,2]. However, because of its extremely low abundance and the increasing demand from various industries, the high cost associated with Pt has become a major barrier to the commercialization of PEMFCs [3]. To make a Pt-based catalyst cost-effective, one has to enhance its catalytic activity while reducing the usage of Pt. Previous work has demonstrated that the catalytic activity of Pt-based catalysts towards the ORR could be greatly enhanced by engineering the exposed catalytic surface structure [4,5], tuning the elemental composition [6–8], constructing a core–shell or hollow nanostructure [9–11], or a combination of these strategies [12–14]. For example, Pt₃Ni octahedra enclosed by {1 1 1} facets have been shown to exhibit

^{*} Corresponding authors

E-mail addresses: Mavrikakis, M. (manos@engr.wisc.edu), Xia, Y. (younan.xia@bme.gatech.edu)

[†] J.Z. and A.O.E. contributed equally to this work.

[‡] Computational work.

[¶] Experimental work.

significantly improved catalytic activity towards ORR relative to $Pt(1\ 1\ 1)$ and $Pt_3Ni(1\ 0\ 0)$ surfaces [15,16]. Recently, we have developed a series of Pd@Pt core–shell nanocrystals with different surface atomic structures, and thus facet-dependent catalytic properties, showing marked enhancements in both activity and durability relative to a commercial Pt catalyst [17–19]. Despite the robust success achieved towards the rational design of such catalysts, they still lack sufficient stability because of the selective electrochemical leaching and/or dissolution of other less stable metals (e.g., Ni and Pd) during accelerated durability tests.

Under ORR conditions, Ir is one of the few elements that is thermodynamically stable and resistant against surface segregation and leaching in acidic environments [20,21]. According to density functional theory (DFT) calculations, when alloying Pt with Ir, especially Pt₄Ir, Pt-OH coverage will decrease, speeding up the sluggish kinetics associated with the ORR relative to pure Pt, due to lateral repulsion between the OH* (* denotes the adsorbed species) adsorbed on surface Pt atoms and the O* and/or OH* adsorbed on neighboring Ir [22]. Benefiting from these intrinsic physicochemical properties and related electronic/synergistic effects, Pt-Ir alloy nanocrystals have been considered as some of the most promising catalysts towards ORR for their substantially enhanced activity and durability [23-27]. However, in further optimizing their catalytic properties, facetcontrolled synthesis of Pt-Ir alloy nanocrystals has been met with limited success [28-30]. To this end, precisely engineering the type of facet exposed on the surface of Pt-Ir alloy nanocrystals, and thus rationally optimizing their performance towards ORR, remains an unmet challenge.

Here we report the facet-controlled synthesis of Pd@Pt–Ir core–shell nanocrystals *via* atomic layer-by-layer co-deposition of Pt and Ir atoms on Pd seeds with different shapes (*e.g.*, cubes, octahedra, and icosahedra). The Pd@Pt–Ir nanocrystals, including cubes, octahedra, and icosahedra, could be readily made with ultrathin Pt–Ir alloy shells of only 1.6-atomic-layer thick with a composition of *ca*. Pt₄Ir to present well-defined and controllable Pt–Ir {1 0 0}, {1 1 1}, and {1 1 1} facets combined with twin boundaries, respectively. When examined as catalysts towards ORR, the Pd@Pt–Ir core–shell nanocrystals exhibited facet-dependent catalytic properties. All of them showed substantially enhanced activity and durability relative to a commercial Pt/C and their Pd@Pt counterparts, with the Pd@Pt–Ir icosahedra exhibiting the maximal activity.

Results and discussion

Synthesis and characterization of Pd@Pt–Ir nanocrystals: We first prepared Pd cubic, octahedral, and icosahedral seeds with average edge lengths of 17.8 ± 3.1 , 20.6 ± 3.2 , and 12.9 ± 1.6 nm (Figs. S1, S2), respectively. Their surfaces were mainly covered by $\{1\ 0\ 0\}$ facets, $\{1\ 1\ 1\}$ facets, and $\{1\ 1\ 1\}$ facets plus twin boundaries, respectively. We then synthesized Pd@Pt–Ir core–shell cubes, octahedra, and icosahedra with an ultrathin Pt–Ir alloy shell of only about 1.6-atomic-layer thick through conformal, layer-by-layer co-deposition of Pt and Ir atoms on the Pd seeds. Specifically, on the basis of similar reduction potentials for Pt (IV)/Pt and Ir(III)/Ir and strong reducing power of ascorbic acid [31], the Pt and Ir atoms were expected to be simultaneously

deposited on the surface of each Pd seed as a conformal shell when a mixed precursor solution containing Pt(IV) and Ir(III) at a molar ratio of 4:1 was slowly $(1\,\mathrm{mL\cdot h^{-1}})$ introduced at 190 °C. A combination of co-reduction and co-deposition at a low injection rate and a high reaction temperature ensured the formation of Pd@Pt–Ir nanocrystals with a fixed shell composition, a uniform shell thickness, and a smooth surface terminated in controllable facets. Although this work is focused on Pd@Pt–Ir nanocrystals with an elemental composition of roughly Pt₄Ir for the shell less than 2-atomic-layer thick, the protocol could be readily extended to Pd@Pt–Ir nanocrystals with other compositions and shell thicknesses. It should be pointed out that, in view of the scarcity and high price of Pd, more earth-abundant and cheaper materials should be used for the core in developing sustainable and cost-effective products.

Fig. 1a-c shows typical transmission electron microscopy (TEM) images of the Pd@Pt-Ir cubes, octahedra, and icosahedra, respectively, revealing good retention of cubic, octahedral, and icosahedral shapes during the synthesis. Fig. 1d-f shows highangle annular dark-field scanning TEM (HAADF-STEM) images taken from an individual Pd@Pt-Ir cube, octahedron, and icosahedron, respectively, suggesting that the surface atomic structures of the respective Pd cores were all devotedly repeated by the Pt-Ir shells for the generation of ordered structures spreading across the surface. The overlayers can be identified owing to the clear contrast between the Pt-Ir shells (brighter) and Pd cores caused by the large difference in atomic number. The atomicresolution HAADF-STEM images (Fig. 1g-i) confirm the presence of about 2 atomic layers of Pt-Ir in the shells of all Pd@Pt-Ir nanocrystals. The lattice spacing of about 0.19 and 0.23 nm can be assigned to the (200) and (111) planes of facecentered cubic Pt/Ir, confirming that the Pd@Pt-Ir cubes and octahedra were enclosed by Pt-Ir {1 0 0} and {1 1 1} facets, respectively. The well-resolved twin planes and a lattice spacing of 0.23 nm in the Pd@Pt-Ir icosahedron suggest that particle was bounded by Pt-Ir {1 1 1} facets with twin boundaries. We also quantitatively analyzed the average number of atomic layers in the shell by using inductively coupled plasma mass spectrometry (ICP-MS). The shells were 1.63, 1.57, and 1.55 atomic layers in thickness, respectively, for the Pd@Pt-Ir cubes, octahedra and icosahedra (Table S1), which were in good agreement with the atomic-resolution HAADF-STEM images. Due to the codeposition of Pt and Ir atoms with the nearly same deposition efficiency of about 80% during a synthesis (Table S1), the molar ratios of Pt to Ir obtained by ICP-MS were 4.14:1, 4.06:1, and 3.95:1 for the Pd@Pt-Ir cubes, octahedra and icosahedra, respectively, in consistency with the feeding ratio of Pt(IV) to Ir(III) precursors. Energy-dispersive X-ray spectroscopy (EDX) mapping (Fig. 1j-l) and X-ray photoelectron spectroscopy (XPS) (Fig. S3) further verified the formation of Pd@Pt-Ir core-shell structures, with the shells composed of metallic Pt and Ir in the form of a Pt-Ir alloy.

During the growth of a core–shell nanocrystal, the relative rates of co-deposition and surface diffusion of Pt and Ir adatoms play a key role in forming a conformal, uniform Pt–Ir shell on the surface of a Pd seed [32]. Similar to the synthesis of the Pd@Pt, Pd@Ir, and Pd@Ru nanocrystals [17,33–35], the surface diffusion could be tuned by varying reaction temperature, while the co-

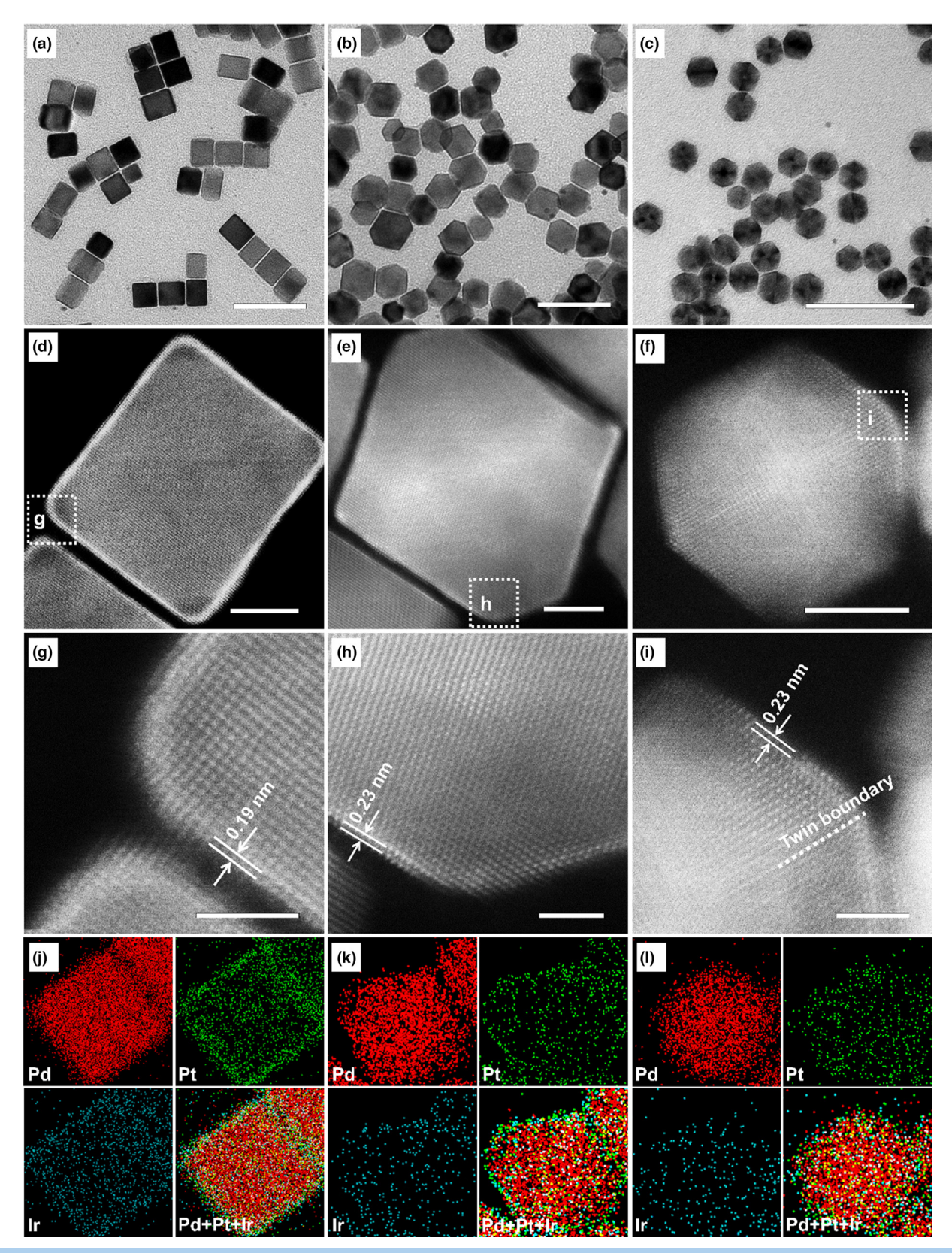


FIGURE 1

TEM images of Pd@Pt-Ir core-shell nanocrystals: (a) cubes, (b) octahedra, and (c) icosahedra (scale bars: 50 nm). HAADF-STEM images of a single (d) cube, (e) octahedron, and (f) icosahedron (scale bars: 5 nm). (g-i) Atomic-resolution HAADF-STEM images taken from the region boxed in (d-f), showing about two atomic layers of Pt-Ir in the shell (with a brighter contrast) and the Pd atoms in the core (scale bars: 2 nm). (j-l) EDX mapping analyses of the distribution of Pd, Pt, and Ir, confirming a core-shell structure and an alloyed shell on each nanocrystal.

deposition was largely dependent on the precursor injection rate and KBr concentration in the growth solution. Taking the growth of Pd@Pt-Ir cubes as an example, when reducing the temperature to 120 °C, the surface diffusion of Pt and Ir adatoms was decelerated, and most of the deposited Pt and Ir atoms tended to stay at the corners and edges, leading to the production of concave cubes (Fig. S4a). When the injection rate was increased to 40 mL·h⁻¹ or no KBr was introduced, we obtained cubic multipods and even small particles with irregular shapes (Fig. S4b, c). In these cases, surface diffusion failed to catch up with the co-reduction and/or co-deposition of Pt and Ir atoms, causing the accumulation of adatoms at the corners, or even the homogeneous nucleation and growth of the atoms.

Electrocatalytic activity of the Pd@Pt–Ir nanocrystals: Because it is well-established that Pd- and Ir-based nanocrystals are much less active than Pt-based nanocrystals towards ORR in acidic media [1,2], in this work, we only benchmarked the ORR electrocatalytic performance of the Pd@Pt–Ir nanocrystals (deposited on Vulcan XC-72 carbon support, Fig. S5) against a commercial Pt/C catalyst. We used cyclic voltammetry (CV) to measure the electrochemical active surface area (ECSA) of each catalyst (Fig. S6a). Attributed to their ultrathin shells of only 1.6-atomic-layer thick, the specific ECSAs of the Pd@Pt–Ir cubes/C, octahedra/C, and

icosahedra/C (93.2, 101.4 and 121.7 m $^2 \cdot g_{Pt+Ir}^{-1}$, respectively) were much higher than that of the commercial Pt/C (59.4 m $^2 \cdot g_{Pt}^{-1}$) (Fig. S6b), even though the sizes of Pd@Pt–Ir nanocrystals were almost 4–7 times as high as that of the Pt particles in commercial Pt/C. Taken together, the dispersion of Pt and Ir can be improved even when switching to larger particles, as long as the Pt and Ir atoms are located into ultrathin overlayers consisting of a few atomic layers only.

Fig. 2a shows the ORR polarization curves of Pd@Pt–Ir/C catalysts, together with that of the commercial Pt/C. We calculated the kinetic currents of the ORR polarization curves according to the Koutecky–Levich equation, and then normalized the kinetic currents against the ECSAs, and the Pt mass and/or the total mass of Pt and Ir to obtain the specific and mass activities (j_k , specific and j_k , mass), respectively. (Fig. 2b and c). Similar to the ORR activity trend of Pd@Pt cubes, octahedra, and icosahedra [17–19], the j_k , specific and j_k , mass of Pd@Pt–Ir/C catalysts showed a direct correlation with the number of {1 1 1} facets and twin boundaries (identified to be favorable for ORR) [36,37], and the activities ranked as follows: Pd@Pt–Ir icosahedra/C > Pd@Pt–Ir octahedra/C > Pd@Pt–Ir cubes/C. Compared to the commercial Pt/C, the j_k , specific and j_k , mass of all the Pd@Pt–Ir/C catalysts were greatly enhanced. Specifically, at 0.9 V, the j_k , specific of the Pd@Pt–

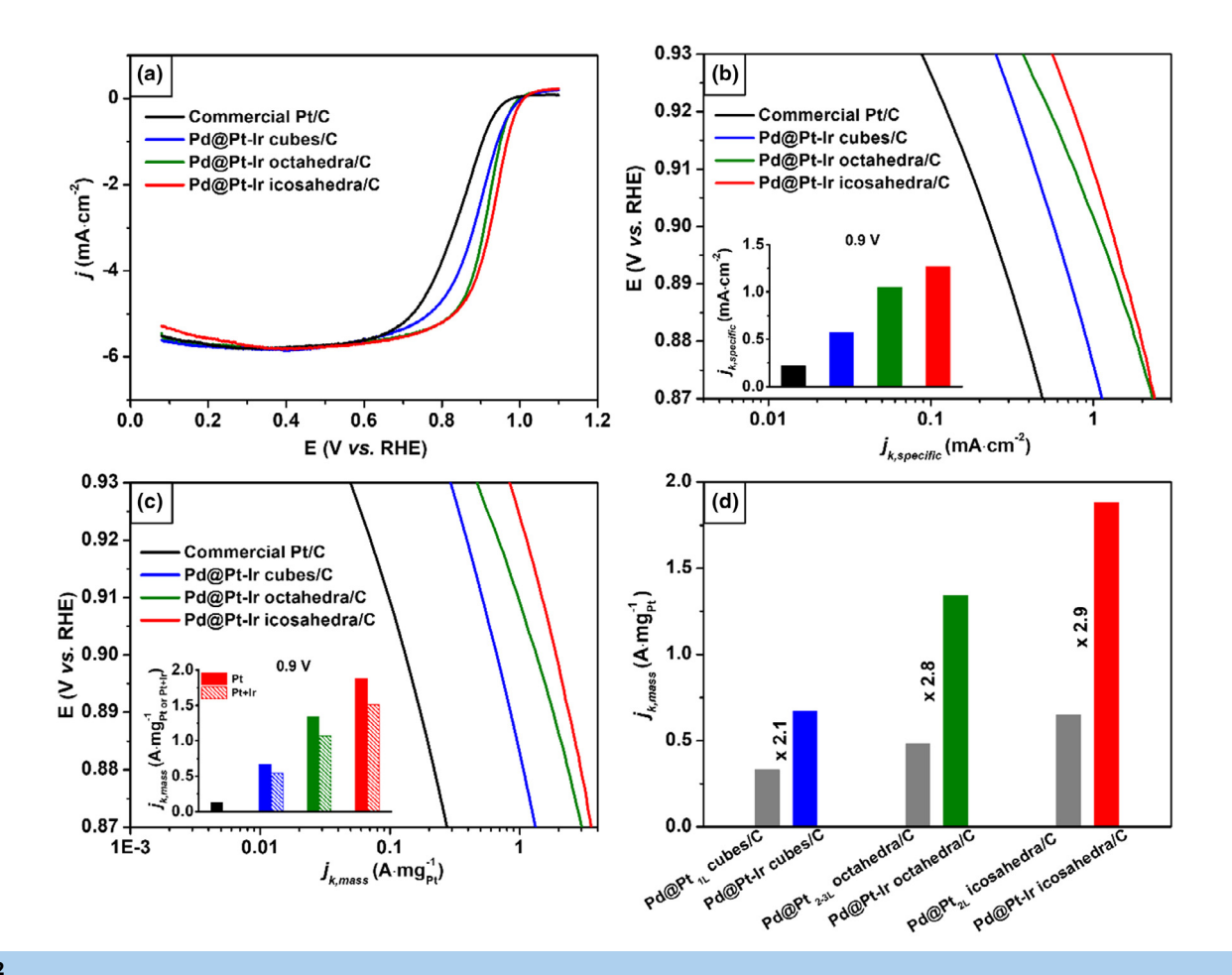


FIGURE 2

(a) ORR polarization curves recorded from the commercial Pt/C, Pd@Pt-Ir cubes/C, Pd@Pt-Ir octahedra/C, and Pd@Pt-Ir icosahedra/C. (b) Specific and (c) mass ORR activities given as kinetic current densities (j_k) normalized to the ECSAs, and Pt and/or Pt + Ir masses of the catalysts, respectively. (d) ORR mass activities at 0.9 V of the Pd@Pt-Ir/C catalysts relative to their Pd@Pt/C counterparts [17–19], highlighting the substantial enhancement in activity (see Table S2 for the details).

Ir cubes/C, octahedra/C, and icosahedra/C (0.57, 1.05, and 1.27 mA·cm⁻², respectively) showed 2.6-, 4.8-, and 5.8-fold enhancements relative to the commercial Pt/C $(0.22 \text{ mA} \cdot \text{cm}^{-2})$. Per Pt mass, the Pd@Pt-Ir cubes/C, octahedra/C, and icosahedra/C had $j_{k, mass}$ of 0.67, 1.34, and 1.88 A·mg $_{Pt}^{-1}$ at 0.9 V, which were almost 5.2, 10.3, and 14.5 times, respectively, as high as that of the commercial Pt/C (0.13 $A \cdot mg_{Pt}^{-1}$). Even when normalized against the total mass of Pt and Ir, the jk, mass of Pd@Pt-Ir cubes/ C, octahedra/C, and icosahedra/C still delivered 4.2-, 8.4-, and 11.6-fold enhancements relative to the commercial reference, respectively. In Fig. 2d, S7 and Table S2, we compare the $j_{k, mass}$ and $j_{k, specific}$ of the Pd@Pt-Ir cubes/C, octahedra/C, and icosahedra/C with those of the previously reported Pd@Pt cubes/C [17], octahedra/C [18], and icosahedra/C [19], revealing greatly enhanced activities towards ORR for the Pd@Pt-Ir/C catalysts. Relative to their Pd@Pt/C counterparts, the Pd@Pt-Ir cubes/C, octahedra/C, and icosahedra/C, respectively, exhibited 2.1-, 2.8-, and 2.9fold enhancement in $j_{k, mass}$ (normalized against the Pt mass) at 0.9 V. It should be noted that, similar to the Pd core promoting the ORR activities of Pd@Pt nanocrystals [17-19], the ligand and strain effects generated by the Pd core should also be able to enhance the ORR activities of the Pd@Pt-Ir nanocrystals. Taken together, the excellent ORR activities of the Pd@Pt-Ir catalysts could be attributed to a combination of a high dispersion for Pt and Ir atoms, and the possible electronic/synergistic effects arising from the Pd core underlying the Pt-Ir surface and the Ir atoms trapped in the Pt lattice. Moreover, one can rationally optimize the catalytic properties of the Pd@Pt-Ir nanocrystals by controlling their surface atomic structure. Speaking of facet effects, it is interesting to note that part of the reason why cubes are inferior to octahedra and icosahedra in terms of activity is unlike on Pd (1 1 1), Pt and Ir may prefer to dig into Pd(1 0 0) and push Pd to the surface of the cubes during synthesis, enriching the surface of a cube with more Pd, a metal that is less active toward ORR than Pt [38].

DFT calculations: To gain a fundamental understanding of the beneficial role of Ir, and to rationalize the facet dependence of the experimentally-observed activities, we performed periodic DFT calculations (GGA-PW91, see the SI for details) for the ORR mechanism on a number of model surfaces reflecting our synthesized nanocrystals [39-41]. Specifically, we employed a simple electrochemical model to calculate the free energies of protonation for adsorbed O* (to form OH*) and OH* (to form H_2O) on the {1 1 1} and {1 0 0} facets of Pt, Pd@Pt_{1L}, Pd@Pt_{2L}, Pd@Pt-Ir_{1L}, and Pd@Pt-Ir_{2L}, where the subscripts 1L or 2L refer to the thickness of the shell on top of the Pd slab [42]. This last category of Pd@Pt-Ir_{2L} encompassed its own family of surfaces (for either facet) which accounted for all possible permutations of the positions of Ir atoms in the predominantly Pt shell (Figs. S8-S11). Since the HAADF-STEM images (Fig. 1) and ICP-MS analysis (Table S1) indicated the presence of ca. 1.6 atomic layers of the shell, we confined our discussion here to surfaces with shells comprised of 2 atomic layers. Furthermore, we confined the discussion regarding the Pd@Pt-Ir_{2L} family to the surfaces with the most energetically-stable permutations under relevant OH* coverage (see SI for details), namely: Pd@Pt-Ir_{2Lb-} $_{b\text{-linear}}$ for the $\{1\,0\,0\}$ facet, in which both Ir atoms in unit cell were in the bottom layer of the shell as nearest neighbor atoms,

and Pd@Pt–Ir_{2Lt-b-near} for the {1 1 1} facet in which both layers of the shell had a single Ir atom with both Ir atoms coordinated to each other in a unit cell. We presented all ORR results on all systems in Tables S3–S5 and the discussion thereof.

We started by reporting the calculated free energies of protonation for O* and OH* at 0.9 V on the Pd@Pt_{2L} $\{1\ 1\ 1\}$ and {1 0 0} surfaces. On the Pd@Pt_{2L} {1 1 1} surface, O* protonation was endergonic by 0.21 eV, while OH* protonation was easier at 0.09 eV. This trend in sequential protonation steps was reversed for the more strongly-binding {100} facet in which O* protonation was facile at 0.06 eV but OH* removal from the surface (i.e., protonation to water) was endergonic by 0.23 eV. Fig. 3 shows the free energy of protonation for the more difficult of the two elementary steps on the Pd@Pt_{2L} surfaces. We then turned our attention to the Pd@Pt-Ir_{2L} surfaces. Examining the data in Table S3, we found two clear, facet-independent trends: i) both protonation steps are, in general, significantly more endergonic than they were on the Pd@Pt_{2L} surfaces, and ii) OH* protonation was more endergonic than O* protonation. This indicates that O* and OH* are significantly more strongly bound to the Pd@Pt-Ir_{2L} surfaces compared to the Pd@Pt_{2L} surfaces. These observations are understandable, given the stronger binding of oxygenated species to Ir as compared to Pt and the propensity of Ir electrodes to form oxides at low potentials [43,44]. Clearly, the high thermodynamic barriers (generally, in excess of 0.50 eV) for the protonation of O* and OH* on Pd@Pt-Ir_{2L} surfaces contradicted the experimentally-measured higher activity of the Pd@Pt-Ir_{2L}/C catalysts relative to the Pd@Pt/C or Pt/C catalysts. These results implied that there was a higher coverage of oxygenated species on the Pd@Pt-Ir_{2L} sur-

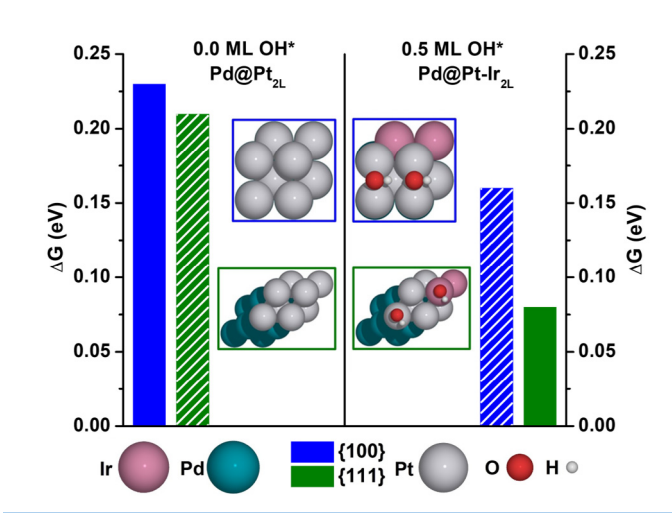


FIGURE 3

Calculated free energy of protonation at 0.9 V for O*and OH* on cubic {1 0 0} (in blue) and octahedral {1 1 1} (in green) facets of Pd@Pt_L and Pd@Pt_Ir_2L surfaces. The Pd@Pt_Ir_2L surfaces shown here are Pd@Pt_Ir_2Lb-b-linear and Pd@Pt_Ir_2Lt-b-near for the {1 0 0} and {1 1 1} facets, respectively (see SI for details). The results for Pd@Pt_L systems are given for clean surfaces, while the results for Pd@Pt_Ir_2L systems are given under 0.5 ML total coverage of OH* spectators. The insets show the working coverages and structures of both systems. Solid bars indicate that the more difficult of the two protonation steps is from OH* to H₂O, while hatched bars indicate that the more difficult of the two protonation steps is from O* to OH*. In the insets, gray, blue, pink, red, and white spheres represent Pt, Pd, Ir, O, and H species, respectively.

faces as compared to the $Pd@Pt_{2L}$ surfaces. More specifically, the fact that OH* protonation was more endergonic than O* protonation on the $Pd@Pt-Ir_{2L}$ surfaces indicated that these surfaces would likely be covered with OH* species, which is in agreement with literature [25]. Taken together, a relevant model for these $Pd@Pt-Ir_{2L}$ surfaces must explicitly include relevant OH* coverage.

We then calculated the free energies of protonation of O* and OH* on Pd@Pt-Ir_{2L} surfaces pre-covered with 0.25 ML and 0.50 ML of OH* spectators (Table S3-S5). Fig. 3 shows the free energies of the more difficult of the two protonation steps under 0.50 ML OH* coverage on Pd@Pt-Ir_{2Lb-b-linear} {1 0 0} and Pd@Pt-Ir_{2Lt-b-near} {1 1 1}. Importantly, lower free energies of protonation correspond to higher activities. The comparison to the corresponding facets of the Pd@Pt2L surfaces is favorable, and a clear trend is revealed: i) for either facet, the Pd@Pt-Ir_{2L} surface is more active than the corresponding Pd@Pt_{2L} counterpart, and ii) for either system (Pd@Pt_{2L} or Pd@Pt-Ir_{2L}), the {1 1 1} facet is more active than the {100} facet. In that order, these qualitative trends explain the beneficial role of Ir, as well as the experimentallyobserved structure sensitivity. This agreement was only found by explicitly modeling relevant OH* coverage on the stronglybinding Pd@Pt-Ir_{2L} surfaces and comparing these results to the corresponding clean Pd@Pt2L surfaces (i.e. "clean" indicates surfaces not pre-covered with OH*). We also showed in Fig. 4 and Table S6 that OH-OH interactions are generally weaker on the Pd@Pt-Ir_{2L} surfaces compared to Pd@Pt_{2L} surfaces, further explaining the high activity of the Pd@Pt-Ir_{2L}/C catalysts, consistent with literature [22,25]. Specifically, the {1 0 0} Pd@Pt-Ir_{2Lb-b-} linear and the {1.1.1} Pd@Pt-Ir_{2Lt-b-near} (the most energeticallystable Pd@Pt-Ir_{2L} surfaces) have OH-OH interaction energies of -0.07 and +0.44 eV relative to Pd@Pt_{2L}(1 0 0) and Pd@Pt_{2L}(1 1 1), respectively. This indicates that OH-OH interaction is marginally

more attractive (by 0.07 eV) on {1 0 0} Pd@Pt–Ir $_{2Lb-b-linear}$ compared to Pd@Pt $_{2L}$ (1 0 0) and is strongly repulsive (by 0.44 eV) on {1 1 1} Pd@Pt–Ir $_{2Lt-b-near}$ compared to Pd@Pt $_{2L}$ (1 1 1). The strongly repulsive OH–OH interaction energies on the {1 1 1} Pd@Pt–Ir $_{2Lt-b-near}$ further explain the higher activity of the octahedra compared to the cubes. These results shed light on the importance of adequate representation of coverage effects in electrocatalysis.

As a final note on activity, we would like to discuss the activity of the Pd@Pt–Ir/C icosahedra, the highest among our surfaces. Both octahedra and icosahedra preferentially expose the more active {1 1 1} facets, but unlike octahedra, the twin boundaries of icosahedra impart tensile strain on the side faces [35]. Previous work has shown that this tensile strain allows for the incorporation of additional Pt atoms in the shell of Pd@Pt icosahedra nanocrystals, thus imparting a net compressive strain on the Pt shell and thereby higher ORR activity [19]. This effect could also account for the higher activity of the Pd@Pt–Ir icosahedra in this work.

Electrocatalytic durability of the Pd@Pt-Ir nanocrystals: In addition to the substantially enhanced specific and mass activities, the Pd@Pt-Ir/C catalysts exhibited superb catalytic durability. We evaluated the catalytic durability of the Pd@Pt-Ir/C catalysts through an accelerated durability test. Judged by the specific ECSAs and mass activities at 0.9 V, the durability of the Pd@Pt-Ir/C was significantly improved relative to the commercial Pt/C as well as their Pd@Pt counterparts even with thicker Pt atomic layers (Figs. 5, S12, S13 and Table S2). After 10,000 cycles of test, the Pd@Pt-Ir/C catalysts only exhibited a 3–9% drop in their specific ECSAs, as opposed to a 35–47% drop for the specific ECSAs of the commercial Pt/C (after 5,000 testing cycles only) and the Pd@Pt counterparts (Fig. 5a and b). At 0.9 V, the mass activities of Pd@Pt-Ir/C catalysts after 10,000 cycles of test

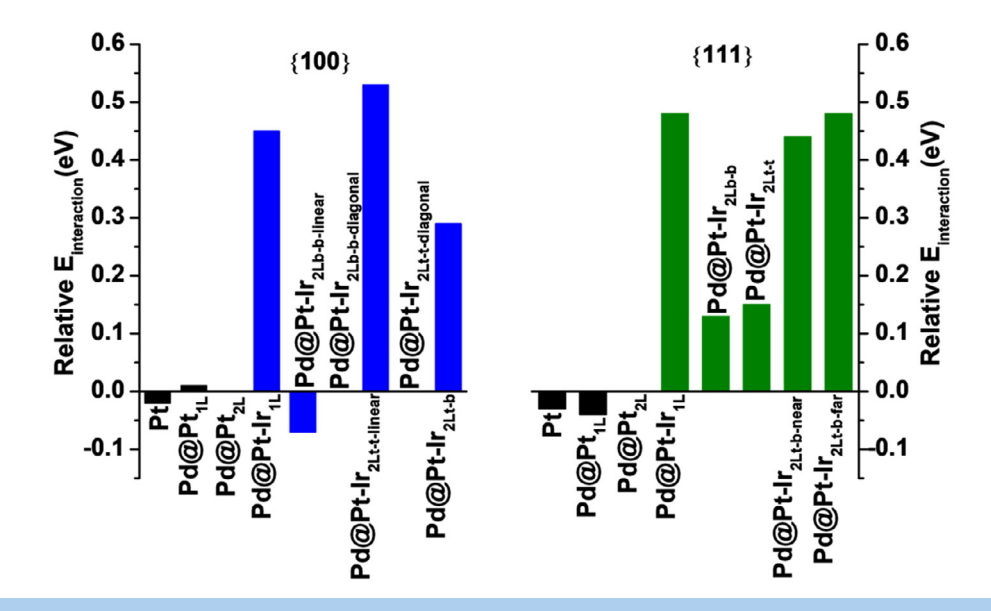


FIGURE 4

OH–OH interaction energies ($E_{interaction}$) on all surfaces relative to the OH–OH interaction energy on the Pd@Pt_{2L} surface (shown with zero relative $E_{interaction}$) for each facet. Positive relative $E_{interaction}$ refers to repulsion or weaker attraction compared to the OH–OH attraction on the Pd@Pt_{2L} surface. Negative relative $E_{interaction}$ refers to stronger attraction compared to the OH–OH attraction on the Pd@Pt_{2L} surface. The total OH* coverage is 0.50 ML, corresponding to a total of two OH* on the surface per unit cell. Blue bars refer to cubic Pd@Pt–Ir_{2L} surfaces, green bars refer to octahedral Pd@Pt–Ir_{2L} surfaces, and black bars refer to Ir-free surfaces (irrespective of facet).

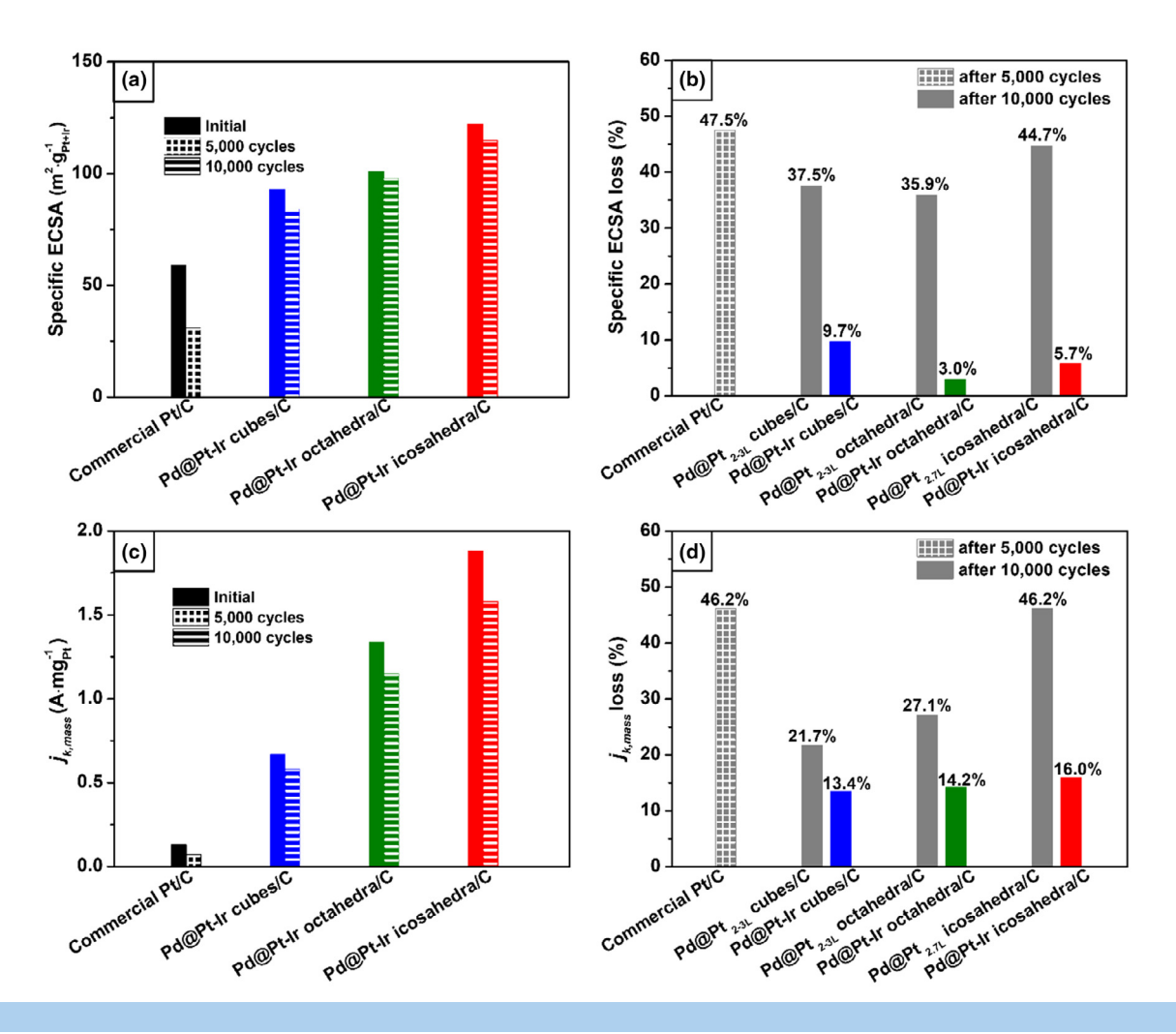


FIGURE 5

(a) Specific ECSAs of the catalysts before and after accelerated durability tests. (b) Losses of the ECSAs of the catalysts after accelerated durability tests. (c) Mass activities of the catalysts at 0.9 V before and after accelerated durability tests. (d) Losses of the mass activities of the catalysts after accelerated durability tests.

showed only 13–16% losses, while the commercial Pt/C, Pd@Pt cubes/C [17], octahedra/C [18], and icosahedra/C [19], exhibited much greater losses of 46% (after 5000 testing cycle only), 22%, 27% and 46%, respectively (Fig. 5c and d). Relative to the pristine Pt/C, after 10,000 testing cycles, the Pd@Pt-Ir cubes/C, octahedra/C, and icosahedra/C still showed 4.5-, 8.8-, and 12.2-fold enhancements in mass activity (normalized against the Pt mass) at 0.9 V. TEM images of the Pd@Pt-Ir catalysts after durability test revealed the favorable structural integrity without any obvious destruction of the Pd cores (Fig. S14), while the Pd cores of the Pd@Pt counterparts underwent severe dissolution and degradation, diminishing the ligand and strain effects and thus causing the activity to decrease [17–19]. This could be attributed in part to the higher resistance of the surface Pt atoms to oxidation (and thus dissolution) in the presence of Ir atoms. The incorporation of a small amount of an oxophilic metal to a Pt monolayer atop a single crystal of Pd(1 1 1) could impart stronger repulsions (relative to a pure Pt monolayer) between oxygenated species, leaving their removal easier on the Pt sites than in the absence of such oxophilic metals [22,25]. As a proof of this concept, we tabulated OH-OH interaction energies on all surfaces in

Table S6, and we showed in Fig. 4 that these interactions were generally repulsive for the Pd@Pt–Ir surfaces compared to Pd@Pt $_{\rm 2L}$, as discussed in more detail above. In essence, this phenomenon raised the oxidation potential of Pt, which was similar to the postulated effect of Au clusters on Pt nanoparticles for the ORR [45]. Taken together, incorporation of Ir atoms into Pt lattice to form a Pt–Ir alloy shell could bring a better passivation of the Pd core, thereby greatly improving the catalytic durability of Pd@Pt–Ir catalysts.

Conclusions

In this work, we have demonstrated a facile synthesis of Pd@Pt–Ir nanocrystals with cubic, octahedral, and icosahedral shapes and further explored their facet-dependent activity and durability towards ORR. These Pd@Pt–Ir nanocrystals present well-defined Pt–Ir {1 0 0} facets, {1 1 1} facets, and {1 1 1} facets plus twin boundaries, respectively, on their surface. For the proof-of-concept study, we have focused on nanocrystals with a shell thickness of 1.6 atomic layers while the elemental composition was controlled at roughly Pt₄Ir. Owing to their favorable merits,

such as high dispersion of Pt and Ir atoms and the coverage effects arising from the Ir atoms incorporated in the Pt lattice, which were further rationalized by our DFT calculations, the Pd@Pt–Ir nanocrystals showed substantial enhancements in both activity and durability towards ORR relative to a commercial Pt/C and their Pd@Pt counterparts, with the Pd@Pt–Ir icosahedra exhibiting the best performance. This work opens the door to the design and rational synthesis of highly-efficient and long-lived electrocatalysts towards ORR.

Experimental methods

Chemicals and materials: The chemicals obtained from Sigma-Aldrich include ascorbic acid (AA, 99%), potassium bromide (KBr, 99%), sodium hexachloroplatinate hexahydrate (Na₂PtCl₆- 6 H₂O, 98%), sodium hexachloroiridate hydrate (Na₃IrCl₆- 4 xH₂O, 99%), sodium tetrachloropalladate (Na₂PdCl₄, 98%), poly(vinyl pyrrolidone) (PVP, MW \approx 55,000), aqueous formaldehyde solution (HCHO) with HCHO concentration of 36.5–38%, diethylene glycol (DEG, 99%), and acetic acid (99.7%). Other chemicals include ethylene glycol (EG, 99%, J. T. Baker), ethanol (200 proof, KOPTEC), and aqueous perchloric acid (HClO₄, PPT Grade, Veritas) solution with a concentration of 70%. All aqueous solutions were made up by using deionized water with a resistivity of 18.2 MΩ·cm⁻¹ at room temperature.

Synthesis of the 10.4-nm and 17.8-nm Pd cubes: In a typical synthesis of 10.4-nm Pd cubes [46], 8 mL of water, 60 mg of AA, 300 mg of KBr, and 105 mg of PVP were introduced into a 20-mL vial and then magnetically stirred and heated at 80 °C in an oil bath for 10 min. Subsequently, 3 mL of Na₂PdCl₄ aqueous solution at a concentration of 19 mg mL⁻¹ was injected into the mixture. The vial was capped and further heated at 80 °C for 3 h. The product was centrifuged and collected, washed twice with water, and then dispersed in water at a concentration of 1.58 mg·mL⁻¹. The 17.8-nm Pd cubes were produced by increasing the amount of KBr from 300 to 600 mg, with all other conditions unchanged. The 17.8-nm Pd cubes were well dispersed in EG at a concentration of 1.38 mg·mL⁻¹.

Synthesis of the 20.6-nm Pd octahedra: In a typical synthesis [47], HCHO (0.1 mL), PVP (105 mg), water (7.66 mL), and 0.34 mL of a suspension of the 10.4-nm Pd cubes were placed in a 20-mL vial and then magnetically stirred and heated at 60 °C for 10 min in an oil bath. Subsequently, an aqueous Na₂-PdCl₄ solution (3 mL) at a concentration of 9.67 mg·mL $^{-1}$ was one-shot added into the pre-heated mixture. The vial was capped and then heated at 60 °C for additional 3 h. The product was centrifuged and collected, washed twice with water, and finally dispersed in EG at a concentration of 0.78 mg·mL $^{-1}$.

Synthesis of the 12.9-nm Pd icosahedra: In a typical synthesis [48], 2.0 mL of DEG containing PVP (80 mg) was placed in a 20-mL vial and then magnetic stirred and heated at 130 °C for 10 min in an oil bath. Subsequently, a $\rm Na_2PdCl_4$ solution in DEG (1 mL) at a concentration of 15.5 mg·mL⁻¹ was one-shot added into the pre-heated mixture. The vial was capped and further heated at 130 °C for 3 h. The final product was centrifuged and harvested, washed once with acetone and twice with DI water, and dispersed in EG at a concentration of 0.85 mg·mL⁻¹.

Synthesis of the Pd@Pt-Ir core-shell nanocrystals: The Pd@Pt-Ir cubes were synthesized through seed-mediated growth. In a standard procedure, a suspension (0.36 mL) of the 17.8-nm Pd cubes, EG (3.5 mL), AA (30 mg), KBr (50 mg), and PVP (50 mg) were placed into a 20-mL vial and then magnetic stirred and heated at 110 °C for 1 h in an oil bath. The reaction temperature was then rapidly raised to 190 °C within 20 min. Subsequently, Na₃-IrCl₆·xH₂O (0.066 mg) and Na₂PtCl₆·6H₂O (0.30 mg) dissolved together in EG (6 mL) were pumped into the reaction solution at a rate of 1.0 mL·h⁻¹. After introducing the solution of the precursors, the vial was further heated at 190 °C for 1 h. The final product was centrifuged and collected, washed once by using acetone and twice with water, and dispersed in 1 mL of water. The Pd@Pt-Ir octahedra and icosahedra were produced by switching 0.36 mL of the suspension of 17.8-nm Pd cubes to 0.64 mL of a suspension of 20.6-nm Pd octahedra and 0.39 mL of a suspension of 12.9-nm Pd icosahedra, respectively, while all other conditions were kept the same.

Structural and compositional analyses: A Hitachi HT7700 microscope operated at 120 kV was used to take transmission electron microscopy (TEM) images of the samples. The metal contents of the samples were measured by inductively coupled plasma mass spectrometry (ICP-MS, NexION 300Q, PerkinElmer). High-angle annular dark field (HADDF) scanning transmission electron microscopy (STEM) and energy-dispersive X-ray spectroscopy (EDX) images were acquired by using an aberration-corrected Hitachi HD-2700 200 kV STEM equipped with a Brüker Quantax 400/S-STEM EDX detector. X-ray photoelectron spectroscopy (XPS) measurements were completed on each sample using a Thermo Scientific K-Alpha spectrometer equipped with an Al $\rm K\alpha$ microfused monochromatized source.

Preparation of the working electrode: In a typical procedure, the Pd@Pt-Ir core-shell nanocrystals (2 mg) and Vulcan XC-72 carbon support (8 mg) were dispersed in 4 and 16 mL of water, respectively, and then mixed in a 50-mL conical flask under ultrasonication at room temperature for 3 h. To make their surface clean, the collected carbon-supported Pd@Pt-Ir nanocrystals (denoted as Pd@Pt-Ir/C) were treated in 10 mL of acetic acid at 60 °C for 3 h and subsequently washed 8 times with ethanol and/or water. After drying, 4.3, 4.9, and 3.3 mg of the Pd@Pt-Ir cubes/C, octahedra/C, and icosahedra/C, respectively, were evenly dispersed in a mixture of 1 mL of isopropanol, 1 mL of water, and 40 µL of 5% Nafion under ultrasonication for 20 min. 20 μL of each suspension was deposited onto a precleaned glassy carbon rotating disk electrode (RDE, Pine Research Instrumentation) with a geometric area of 0.196 cm² and then dried at 50 °C in an oven. According to ICP-MS analysis, the loading amounts of Pt for all of the Pd@Pt-Ir/C catalysts on RDEs were 6 μg·cm⁻². A commercial Pt/C catalyst (20 wt% 3.2 nm Pt particles on Vulcan XC-72 carbon support, Premetek Co.) was used as a reference for benchmarking purposes. Similar to the Pd@Pt-Ir/C catalysts, 4.0 mg of the commercial Pt/C was well dispersed in a mixture of 2.0 mL of isopropanol, 2.0 mL of water, and 80 µL of 5% Nafion under ultrasonication for 20 min. 10 μL of the suspension was deposited on a pre-cleaned glassy carbon RDE and dried at 50 °C. As determined by ICP-MS, the loading amount of Pt on RDE for Pt/C catalyst was 10 μg·cm⁻².

Electrochemical measurements: A CHI 600E potentiostat (CH Instruments) and glassy carbon RDEs were applied to conduct electrochemical measurements. We used a Pt wire and a Hydro-Flex hydrogen reference electrode (Gaskatel) as the counter and reference electrodes, respectively. All potentials were obtained with reference to the reversible hydrogen electrode (RHE). We measured the cyclic voltammetry (CV) curves in a N2-saturated 0.1 M HClO₄ solution at room temperature in the potential range of 0.08–1.1 V at a scanning rate of 50 mV·s⁻¹. We calculated the electrochemically active surface area (ECSA) of each catalyst on the basis of the charges associated with the desorption of hydrogen in the potential range of 0.08-0.45 V after double-layer correction, with the reference values of 210 μC·cm⁻² for the commercial Pt/C and Pd@Pt-Ir cubes/C, and 240 μC·cm⁻² for the Pd@Pt-Ir octahedra/C and icosahedra/C, respectively. We recorded the oxygen reduction reaction (ORR) polarization curves in an O2-saturated 0.1 M HClO4 solution at room temperature in the potential range of 0.08-1.1 V by the RDE method (with a rotating rate of 1600 rpm) at a scanning rate of 10 mV·s⁻¹. The background current was measured in a N₂saturated 0.1 M HClO₄ solution, while all other conditions were kept the same. We corrected all of the ORR curves by removing the background currents and ohmic iR drop compensation. We performed the accelerated durability tests via CV in the potential range of 0.6-1.1 V for 5,000 and 10,000 cycles at room temperature in an O2-saturated 0.1 M HClO4 solution at a speed of $0.1 \text{ V} \cdot \text{s}^{-1}$.

Acknowledgments

This work was supported in part by a grant from the National Science Foundation (CHE 1804970) and start-up funds from the Georgia Institute of Technology. As a visiting Ph.D. student, J.Z. was also partially supported by fellowships from the China Scholarship Council (CSC) and Nanjing Tech University. Calculations were performed at supercomputing centers located at the Center for Nanoscale Materials at Argonne National Laboratory, supported by DOE contract DE-AC02-06CH11357 and the National Energy Research Scientific Computing Center (NERSC), a DOE Office of Science User Facility supported by DOE contract DE-AC02-05CH11231. Additionally, this research was performed using the computer resources and assistance of the UW-Madison Center for High Throughput Computing (CHTC) in the Department of Computer Sciences. The CHTC is supported by UW-Madison, the Advanced Computing Initiative, the Wisconsin Alumni Research Foundation, the Wisconsin Institutes for Discovery, and the National Science Foundation, and is an active member of the Open Science Grid, which is supported by the National Science Foundation and the U.S. Department of Energy's Office of Science.

Data availability

All data needed to evaluate the conclusions in the paper are present in the paper and/or the Supplementary Materials. Additional data related to this paper may be requested from the authors.

Appendix A. Supplementary data

Supplementary data to this article can be found online at https://doi.org/10.1016/j.mattod.2019.11.002.

References

- [1] M.K. Debe, Nature 486 (2012) 43.
- [2] Z.W. Seh et al., Science 355 (2017) eaad4998.
- [3] A. Rabis, P. Rodriguez, T.J. Schmidt, ACS Catal. 2 (2012) 864.
- [4] B. Lim et al., Science 324 (2009) 1302.
- [5] M. Li et al., Science 354 (2016) 1414.
- [6] X. Huang et al., Science 348 (2015) 1230.
- [7] V.R. Stamenkovic et al., Nat. Mater. 6 (2007) 241.
- [8] D.F. Van Der Vliet et al., Nat. Mater. 11 (2012) 1051.
- [9] L. Zhang et al., Science 349 (2015) 412.
- [10] D. Wang et al., Nat. Mater. 12 (2013) 81.
- [11] C. Chen et al., Science 343 (2014) 1339.
- [12] X. Yang et al., Nano Lett. 16 (2016) 6644.
- [13] L. Bu et al., Science 354 (2016) 1410.
- [14] J. Li et al., Nat. Energy 2 (2017) 17111.
- [15] X. Huang et al., Adv. Mater. 25 (2013) 2974.
- [16] S.-I. Choi et al., Nano Lett. 13 (2013) 3420.
- [17] S. Xie et al., Nano Lett. 14 (2014) 3570.
- [18] J. Park et al., ACS Nano 9 (2015) 2635.
- [19] X. Wang et al., Nat. Commun. 6 (2015) 7594.
- [20] G.E. Ramírez-Caballero et al., Phys. Chem. Chem. Phys. 12 (2010) 2209.
- [21] A.L. Strickler, A. Jackson, T.F. Jaramillo, ACS Energy Lett. 2 (2016) 244.
- [22] J. Zhang et al., J. Am. Chem. Soc. 127 (2005) 12480.
- [23] R. Loukrakpam et al., ACS Catal. 1 (2011) 562.
- [24] S.J. Hwang et al., Chem. Commun. 46 (2010) 8401.
- $\cite{M.B.}$ Vukmirovic et al., Electrochim. Acta 52 (2007) 2257.
- [26] T. Yang et al., ACS Appl. Mater. Interface 8 (2016) 23646.
- [27] M. Zeng et al., J Power Sources 264 (2014) 272.
- [28] C. Zhong et al., Sci. China Mater. 57 (2014) 13.
- [29] T. Zhang et al., Nanoscale 9 (2017) 1154.
- [30] S. Lu et al., J. Mater. Chem. A 5 (2017) 9107.
- [31] K.D. Gilroy et al., Chem. Rev. 116 (2016) 10414.
- \cite{A} X. Xia et al., Proc. Natl. Acad. Sci. USA 110 (2013) 6669.
- [33] M. Zhao et al., Nano Lett. 16 (2016) 5310.
- [34] X. Xia et al., J. Am. Chem. Soc. 136 (2014) 10878.
- [35] J. Zhu et al., Chem. Mater. 31 (2019) 5867.
- [36] J. Wu et al., J. Am. Chem. Soc. 134 (2012) 11880.
- [37] X. Sun et al., ACS Nano 9 (2015) 7634.
- [38] L. Roling, M. Mavrikakis, Nanoscale 9 (2017) 15005.
- [39] G. Kresse, J. Furthmüller, Phys. Rev. B 54 (1996) 11169.
- [40] G. Kresse, J. Furthmüller, Comp. Mater. Sci. 6 (1996) 15.
- [41] J.P. Perdew, Y. Wang, Phys. Rev. B 45 (1992) 13244.
- [42] J.K. Nørskov et al., J. Phys. Chem. B 108 (2004) 17886.[43] I.A. Herron et al., ACS Catal. 4 (2014) 4434.
- [44] T. Reier, M. Oezaslan, P. Strasser, ACS Catal. 2 (2012) 1765.
- [45] J. Zhang et al., Science 315 (2007) 220.
- [46] M. Jin et al., Nano Res. 4 (2011) 83.[47] M. Jin et al., Energy Environ. Sci. 5 (2012) 6352.
- [48] T. Lv et al., ChemSusChem 6 (2013) 1923.